Auto-Tuning of Droop Controllers for Grid-Forming Inverters

Xiangchen Zeng, *Student Member, IEEE,* Tommaso Caldognetto, *Senior Member, IEEE,* Diego Rigato, *Student Member, IEEE,* Andrea Lauri, *Student Member, IEEE,* Davide Biadene, *Senior Member, IEEE*, and Qing Liu, *Member, IEEE*

***Abstract*—This article proposes an auto-tuning control strategy for the power loop of grid-forming inverters to compensate the dynamic performance degradation caused by the variation of unknown variables (e.g., grid impedance, inverter parameter values) under grid-connected operating conditions. The auto-tuning is achieved by online monitoring the crossover frequency and phase margin of the power control loop, and adjusting key parameters of the droop controller according to these performance indices. It is shown that the crossover frequency and phase margin can be maintained at desired values, thus the expected dynamic control performance can be achieved and maintained. Simulation and experimental results are presented to demonstrate the effectiveness of the proposed approach.**

***Index Terms*—Auto-tuning, droop control, grid-forming inverter, lead-lag filter.**

I. Introduction

DRIVEN by the high penetration of distributed energy resources in electrical grids, grid-forming (GFM) capabilities are increasingly required in grid-connected inverters to support frequency and voltage regulation while providing virtual inertia [1]–[3]. Several GFM control schemes have been reported in the literature [4]–[6], typically based on P-f and Q-V relations that link the frequency and amplitude of a voltage-controlled inverter's reference with the generated active and reactive powers, respectively.

Some GFM control schemes are often augmented with inertia emulation to mitigate frequency deviations and high rates of change of frequency [7], as done in the so-called virtual synchronous generators (VSGs). Typically, a low-pass filter (LPF) is added to the power control loops to filter the instantaneous powers and estimate the active and reactive powers corresponding to the fundamental components [8]. It has been shown that the added LPF can also emulate virtual inertia which is equivalent to VSG's emulation [9]. It is worth noting that, in addition to LPFs, lead-lag filters (LLFs) can also be used for implementing the power controllers of GFMs. For example, a configurable natural droop (CND) controller is proposed in [10], which was proven to be an LLF-based power controller [11]. The LLF-based power controller is also used in [12], which presents an alternative implementation to [10]. Besides, the LLF can be directly added to the active-power feedback path of VSGs to improve damping performance [13]. A specific implementation of a droop controller based on an LLF is presented in [14], where the implementation is devised to ease access to the filter parameters, thereby enabling LLF adaptability and the auto-tuning of the power control loop. In contrast to traditional LPF-based droop and VSG schemes, the LLF-based droop controller introduces an additional degree of freedom in its control parameters. By utilizing three distinct parameters, it can independently emulate inertia, damping, and droop characteristics. This enhanced flexibility is instrumental in meeting the diverse functional requirements of GFM inverters [10].

Considering frequency regulation capability and dynamic performance optimization of the power loop, several adaptive control strategies of grid-forming inverters have been proposed. An adaptive virtual inertia strategy is proposed in [15], which can adjust online the virtual inertia based on the observed frequency variations to improve dynamic frequency regulation performance. Reference [16] proposes an adaptive control strategy for VSG, which can automatically adjust the virtual inertia and the damping coefficient to suppress oscillations of frequency and power. Similarly, a self-adaptive inertia-and-damping combination control is proposed in [17] to improve frequency supporting capability. A dual-adaptivity inertia control strategy is proposed to achieve the balance between power regulation and frequency regulation according to different operating conditions in [18]. Reference [19] proposes an intelligent variable droop coefficient estimation method utilizing a novel neural network controller to dynamically adjust parameters in islanded microgrids, effectively suppressing power and frequency fluctuations and improving transient performance under sudden load variations. In addition, [20] proposes a grid-agnostic, adaptive droop control strategy for low-voltage microgrids that dynamically adjusts the reactive droop coefficient based on real-time damping estimations to optimize reactive power sharing while maintaining system stability.

As outlined by the reported literature, most of the adaptive control strategies for grid-forming inverters focus on virtual inertia and the damping properties to improve frequency regulation capability and suppress power oscillations. However, the performance of grid-forming inverters is determined by power controller settings, which are rarely addressed in a systematic manner. Further, existing adaptive control strategies are designed based on a fixed power transfer model, neglecting system parameter variations that degrade performance. To overcome these limitations, an auto-tuning technique for power control of grid-forming inverters is proposed in this article capable of adapting to uncertainty factors (e.g., variation of

grid impedance and inverter parameters) while maintaining desired control performance.

The proposed auto-tuning strategy comprises two stages. First, two control performance indexes, namely, the crossover frequency and the phase margin, of the droop control loop are monitored online to assess the actual performance and capture performance degradations caused by parameter variations in the power loop. Second, the droop controller parameters are adaptively adjusted based on the monitored performance indexes. Eventually, the two performance indexes can be maintained at the targeted values, ensuring the desired control performance of the droop controller.

This paper is based on the preliminary results presented in [14], where the auto-tuning concept with an adaptive implementation of the LLF was first introduced. These contributions are extended herein with additional developments that can be summarized as:

1) presenting the implementation and parameters design of LLF-based droop controllers;
2) redesigning the performance monitor to enhance monitoring capability under severe power variations;
3) presenting the incorporation of decoupled control in the auto-tuner, enabling consistent controller design and improved effectiveness;
4) discussing the practical interpretation of crossover frequency and phase margin in terms of inertia and damping ratio.

In the following, Sect. II recalls fundamental ac power flow relations between two voltage sources and presents the implementation and parameter design of an LLF-based droop controller; Sect. III describes the principles of the proposed auto-tuning strategy together with the design of the performance monitor and the auto-tuner; Sect. IV presents a practical interpretation of the parameters crossover frequency and phase margin in lead-lag droop control. Sect. V shows simulation and experimental results for validation. Sect. VI concludes the paper.

II. Droop Controller with Lead-Lag Filter

A. Preliminary AC Power Transfer Modeling

This subsection recalls the notation and relations for ac power transfer modeling used hereinafter. Fig. 1 schematizes the connection of a three-phase inverter to a grid via an impedance Z_g, where $V_i\angle\delta$ and $V_g\angle 0$ are the inverter and the grid voltage phasors, respectively, and δ is the phase difference between the two voltage sources. The typical case of mainly inductive interconnection impedance is assumed, with Z_g equal to jX_g=$j\omega_g L_g$. If necessary, this assumption is commonly satisfied by control provisions, like the use of virtual inductors added at the inverter output [21], [22].

The power flow-equation can be written as:

$$S = 3\frac{V_i V_g \sin\delta}{X_g} + 3j\frac{V_i}{X_g}\left(V_i - V_g\cos\delta\right) = P + jQ \quad (1)$$

Commonly, δ and $\Delta V_i \triangleq V_i - V_g$ are small due to the small voltage drops along the distribution lines with respect to the nominal grid voltage. As done in other studies focusing on small signals [23] but also transient behaviors [1], [24], by linearizing about $\delta \simeq 0$ and $\Delta V_i \simeq 0$, from (1), it yields:

$$P \approx 3\frac{V_g^2}{X_g}\delta\,, \quad Q \approx 3\frac{V_g}{X_g}\Delta V_i\,, \quad (2)$$

namely, the linearized power-exchange model for Fig. 1. These relations with the transfer function of the active-power droop controller G_P, as in [25], model the active power loop in Fig. 2. G_P may consist in a static term or a dynamic relation, while ω_0 is the nominal angular grid frequency. It is worth noting that this study focuses on the fundamental single-inverter infinite-bus scenario to clearly demonstrate the proposed auto-tuning technique and implementation under operation connected to an electricity grid. Dynamics associated with multi-converter interactions or transient behaviors during severe system faults under islanded operation are addressed in the literature (see, e.g., [24], [26]) and fall beyond the scope of this work.

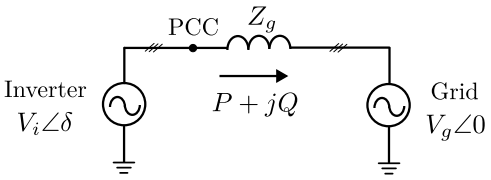

Fig. 1. Simplified diagram of a three-phase grid-tied voltage-controlled inverter.

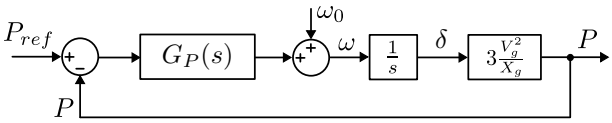

Fig. 2. Small-signal model of the droop active power control loop.

B. Droop Controller with Lead-Lag filter

The LLF-based droop controller proposed in [14] is adopted in this article and the implementation is presented in Fig. 3. As shown in Fig. 3, the LPF is constructed by a unity-gain negative-feedback of an integrator with gain ω_p. This LPF is then multiplied by a coefficient K_1 and another branch with gain K_2 is summed with it. At the end, the resulting transfer function of the LLF-based droop controller is:

$$G_{LLF}(s) = \frac{\omega_p}{s+\omega_p}K_1 + K_2 = (K_1+K_2)\,\frac{s/\omega_z + 1}{s/\omega_p + 1} \quad (3)$$

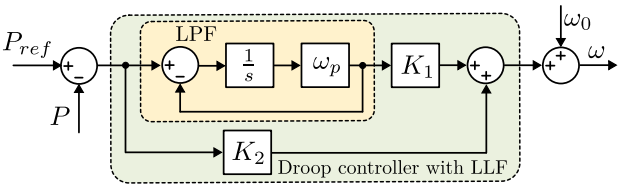

Fig. 3. Lead-lag filter (LLF) implementing G_P of Fig. 2. The displayed structure allows adaptation as described in Sect. III.

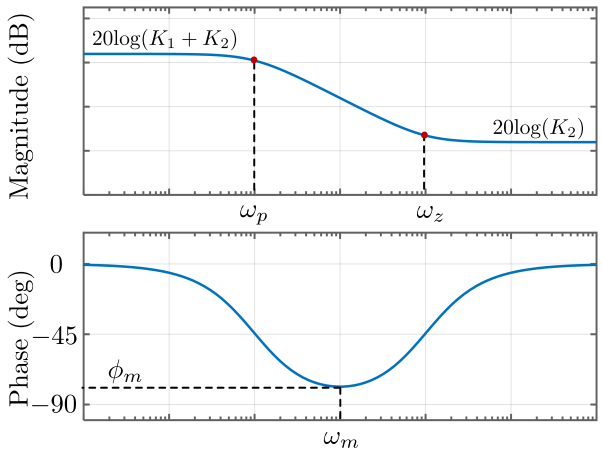

Fig. 4. Bode diagram of the LLF-based droop controller G_{LLF}.

where ω_z and ω_p are the zero and pole frequencies of the LLF. The frequency ω_z can be expressed relative to ω_p as:

$$\omega_z = \omega_p \left(\frac{K_1}{K_2} + 1 \right) \tag{4}$$

From Fig. 2, the active-power loop-gain is $G_P(s) \cdot P(s)/\omega(s)$, that is, using the LLF-based droop controller:

$$T_{LLF}(s) = G_{LLF}(s) \cdot \frac{1}{s} \cdot \frac{3V_g^2}{X_g} \tag{5}$$

which includes the parameters K_1, K_2, ω_p, to be designed.

Fig. 4 displays a typical qualitative Bode diagram of the droop controller in (3), with highlighted the frequencies associated to the pole and the zero of the LLF. From the phase-frequency curve, the minimum phase value ϕ_m (i.e., the maximum phase-lag) occurs at ω_m, which is the geometric mean of the pole frequency and the zero frequency:

$$\omega_m = \sqrt{\omega_p \omega_z} = \omega_p \sqrt{\frac{K_1}{K_2} + 1} \tag{6}$$

in addition, ϕ_m and K_1, K_2 are related as follows [27]:

$$\sin \phi_m = \frac{-K_1}{2K_2 + K_1} \tag{7}$$

From a design point of view, the droop coefficient is typically imposed by the expected grid-frequency range and the nominal power of the inverter [8]:

$$K_p = \frac{\Delta\omega_{\max}}{\Delta P_{\max}} \tag{8}$$

The corresponding static gain of the droop controller (3) is:

$$K_1 + K_2 = K_p = \frac{\Delta\omega_{\max}}{\Delta P_{\max}} \tag{9}$$

By combining (7) and (9), K_1 and K_2 can be obtained:

$$K_1 = K_p \frac{-2 \sin \phi_m}{1 - \sin \phi_m} \quad \text{and} \quad K_2 = K_p \frac{1 + \sin \phi_m}{1 - \sin \phi_m} \tag{10}$$

The parameter ω_p can be designed based on the virtual inertia J and droop coefficient K_p, as shown in [9], [16]:

$$\omega_p = \frac{1}{J\, K_p \omega_0} \tag{11}$$

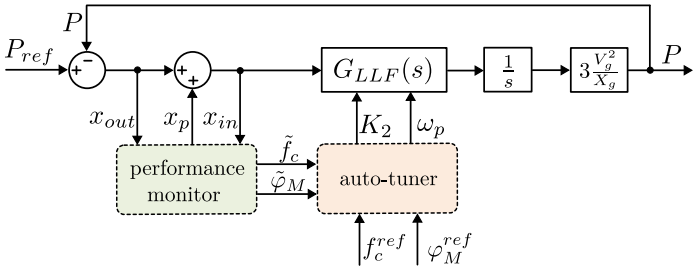

Fig. 5. Schematic overview of the proposed auto-tuning strategy.

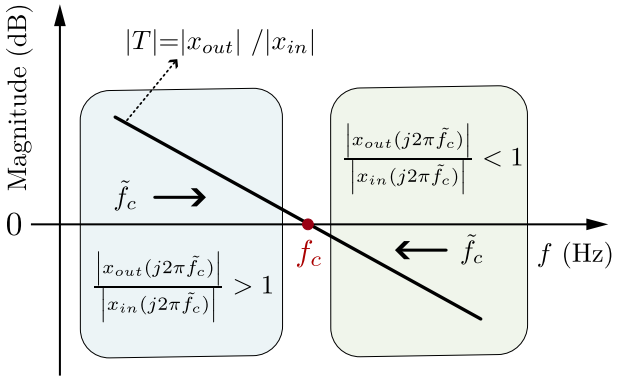

Fig. 6. Estimation of the crossover frequency of a generic loop gain T.

III. Proposed Auto-Tuning Strategy

Fig. 5 displays the proposed auto-tuning strategy. It is composed of two functional blocks (i.e., stages) performed concurrently and online. The first step is monitoring the droop control behavior by a performance monitor. The second step is the automatic adjustment (i.e., auto-tuning) of key droop control loop parameters, which is performed by the auto-tuner.

A. Performance Monitoring

The monitoring technique is based on the Middlebrook's loop gain measurement [28]. As visible in Fig. 5, a small-signal perturbation x_p at frequency $\tilde{f}_c$ generated by the performance monitor is injected into the droop control loop. The frequency response signals before (x_{in}) and after (x_{out}) the injection point are extracted and feed back to the monitor. According to the Middlebrook's loop gain measurement technique, the loop gain T_{LLF} at the frequency $\tilde{f}_c$ can then be estimated by evaluating the ratio of the phasors representing the signals x_{out} and x_{in}, that is:

$$T_{LLF}(j2\pi\tilde{f}_c) = -\frac{x_{out}(j2\pi\tilde{f}_c)}{x_{in}(j2\pi\tilde{f}_c)} \tag{12}$$

Notably, when the injected perturbation frequency is equal to the actual crossover frequency of the loop under test (i.e., when $\tilde{f}_c = f_c$), the unity gain condition is achieved, namely:

$$\left| T_{LLF}(j2\pi\tilde{f}_c) \right| = \frac{\left| x_{out}(j2\pi\tilde{f}_c) \right|}{\left| x_{in}(j2\pi\tilde{f}_c) \right|} = 1, \quad \text{when} \quad \tilde{f}_c = f_c \tag{13}$$

Therefore, the crossover frequency of the droop control loop f_c can be estimated by adjusting the perturbation signal's

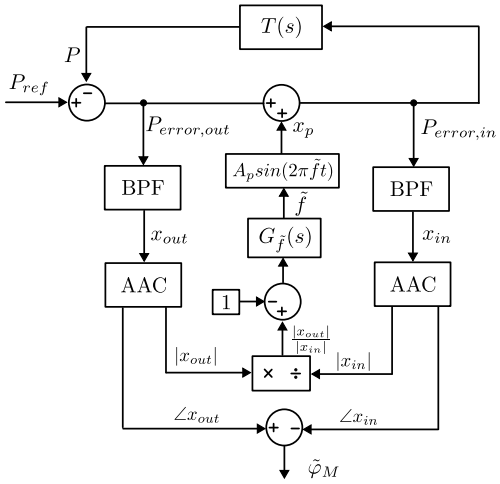

Fig. 7. Structure of the performance monitor.

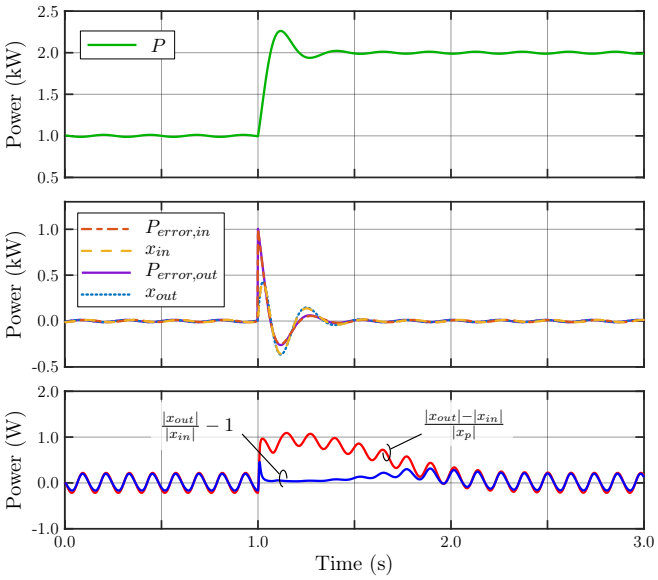

Fig. 8. Monitor's waveforms under power step change considering alternative techniques for the identification of condition (13).

frequency $\tilde{f}_c$ until (13) is satisfied [29]. Fig. 6 illustrates the principle of estimating the crossover frequency. When $\frac{|x_{out}(j2\pi\tilde{f}_c)|}{|x_{in}(j2\pi\tilde{f}_c)|} > 1$ [i.e., $|x_{out}(j2\pi\tilde{f}_c)| > |x_{in}(j2\pi\tilde{f}_c)|$], the perturbation frequency $\tilde{f}_c$ is decreased to approach the actual crossover frequency f_c. On the contrary, when $\frac{|x_{out}(j2\pi\tilde{f}_c)|}{|x_{in}(j2\pi\tilde{f}_c)|} < 1$, $\tilde{f}_c$ is increased to search f_c.

At the estimated unity-gain frequency, the phase margin of the droop control loop $\tilde{\varphi}_M$ can be estimated too, as follows:

$$\begin{aligned}\tilde{\varphi}_M &= \pi + \angle T_{LLF}(j2\pi\tilde{f}_c) \\ &= \angle x_{out}(j2\pi\tilde{f}_c) - \angle x_{in}(j2\pi\tilde{f}_c)\end{aligned} \tag{14}$$

In fact, the estimated phase margin $\tilde{\varphi}_M$ is equal to the actual phase margin φ_M when $\tilde{f}_c = f_c$.

Fig. 7 illustrates the implementation of the approach. $T(s)$ is the active power loop gain under test. Two band-pass filters (BPF) are adopted to extract the frequency response signals (i.e., x_{in} and x_{out}) from the power control loop and attenuate frequency components that are not relevant. The function block amplitude and angle calculation (AAC) is designed to calculate those parameters for the signals x_{in} and x_{out}; additional details on the AAC can be found in [29]. The amplitude ratio between x_{out} and x_{in} (i.e., $|x_{out}|/|x_{in}|$) is used to steer the adjustment of the injected frequency $\tilde{f}$, with control objective (13). A PI regulator $G_{\tilde{f}}$ is adopted to regulate the adjustment of the perturbation frequency $\tilde{f}$ based on the error $1 - |x_{out}|/|x_{in}|$. Then, the small-signal perturbation $x_p = A_p \sin(2\pi\tilde{f}t)$, of amplitude $|x_p| = A_p$, can be generated and injected into the power loop.

Notably, in contrast to other implementations like [29] that use the amplitude difference (i.e., $|x_{out}| - |x_{in}|$) to steer the adjustment process, the amplitude ratio $|x_{out}|/|x_{in}|$ is adopted here to improve the monitor's transient performance under severe variations (e.g., the step change of active power). For example, when a step change is applied on the reference of active power, the signals of extraction points, namely, $P_{error,out}$ and $P_{error,in}$ in Fig. 7, will also present severe fluctuations. Even with the BPF, these fluctuations will inevitably affect the signals x_{out} and x_{in}, eventually leading to inaccurate amplitude estimations of $|x_{out}|$ and $|x_{in}|$. Furthermore, the perturbation frequency adjustment process may experience undesired transients and even risk instability of the monitoring loop.

Compared with amplitude difference, the amplitude ratio is decoupled from the amplitude of the perturbation, which allows better accuracy across transients. Fig. 8 compares the responses of $|x_{out}|/|x_{in}|$ and $|x_{out}| - |x_{in}|$ to a power step change. A fixed crossover frequency is injected into the loop for the simplicity of testing. To ensure fairness of comparison, normalized quantities $|x_{out}|/|x_{in}| - 1$ and $(|x_{out}| - |x_{in}|)/|x_p|$ are displayed, which should ideally be zero under this configuration. The obtained results in Fig. 8 show that the ratio-based index remains close to zero across the step, while the difference-based index exhibits additional undesired fluctuations. Hence, adopting $|x_{out}|/|x_{in}|$ provides better ride-through capability during transients for the proposed monitor.

As typical of active parameter estimation methods, the continuous injection of the perturbation x_p ensures reliable estimations but inevitably introduces oscillations in the plant quantities. Still, the required perturbation amplitude A_p is small: 1%–3% of rated power is shown and experimentally demonstrated in this article, which gives negligible impact under grid-connected operation. For sensitive systems, solutions can be adopted to further limit the impact; these include implementing an automatic amplitude controller to finely minimize the perturbation amplitude, as done in [30] for monitoring purposes, or activating the proposed auto-tuning technique only when needed, as in case of detection of significant parameter variations or system disturbances.

B. Auto-Tuning

Once the control performance indexes are monitored accurately, the auto-tuning process can be implemented. As

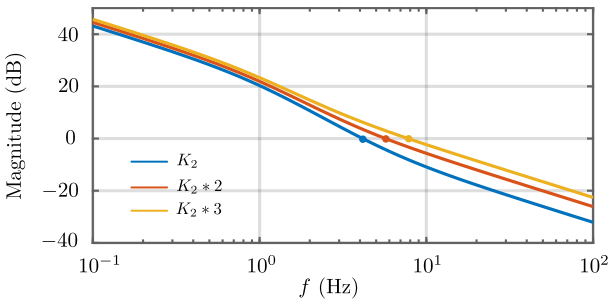

Fig. 9. Magnitude-frequency curve of active power loop gain under different values of K_2.

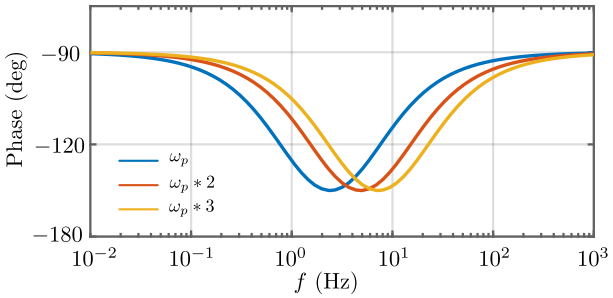

Fig. 10. Phase-frequency curve of active power loop gain under different values of ω_p.

described in Fig. 5, an auto-tuner is designed to adjust the parameters of the droop controller based on the online monitored crossover frequency and phase margin.

1) Tuning of crossover frequency: Fig. 9 presents the magnitude-frequency curve of active power loop gain under different values of K_2. The variation of K_2 obviously affects the magnitude behaviour of the active-power loop gain, thus changing the crossover frequency f_c of the loop gain. Hence, f_c is chosen to steer the adjustment of K_2.

2) Tuning of phase margin: the effect of ω_p on the phase behaviour of the active-power loop gain $T_{LLF}(s)$ is shown in Fig. 10. The two variables are correlated, which allows conditioning the phase margin φ_M by adjusting ω_p.

3) Decoupling of control variables: despite the remarked correlation, some coupling may exist between f_c and ω_p, and between φ_M and K_2, which can impair the effectiveness of the auto-tuning. To optimize tuning performance, a decoupling matrix is employed by analyzing the variations in the performance indexes f_c and φ_M with respect to variations in the droop controller parameters K_2, ω_p of the linearized model of the plant controlled by the auto-tuner. By denoting the variables variations using a hat $\hat{\cdot}$, the following first-order

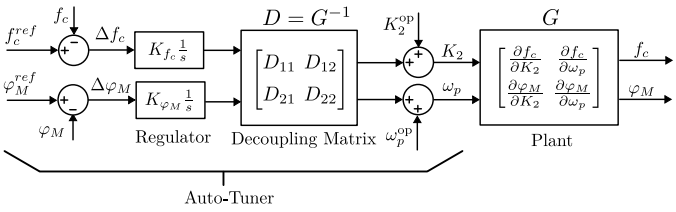

Fig. 11. Block diagram of auto-tuner with decoupling matrix

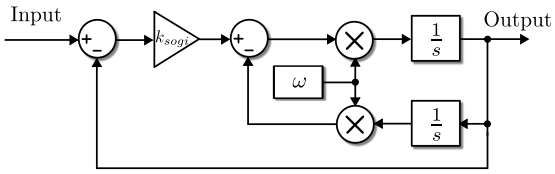

Fig. 12. Structure of the BPF in Fig. 7.

relation is obtained:

$$\begin{bmatrix}\hat{f}_c\\ \hat{\varphi}_M\end{bmatrix} = \begin{bmatrix}\frac{\partial f_c}{\partial K_2} & \frac{\partial f_c}{\partial \omega_p}\\ \frac{\partial \varphi_M}{\partial K_2} & \frac{\partial \varphi_M}{\partial \omega_p}\end{bmatrix}\Bigg|_{\text{op}} \cdot \begin{bmatrix}\hat{K}_2\\ \hat{\omega}_p\end{bmatrix} = G|_{\text{op}} \cdot \begin{bmatrix}\hat{K}_2\\ \hat{\omega}_p\end{bmatrix} \quad (15)$$

which holds around the operating point $\text{op} = \left(K_2^{\text{op}}, \omega_p^{\text{op}}\right)$. A decoupling matrix D is derived as the inverse of $G|_{\text{op}}$, namely, $D = G^{-1}$. The resulting equivalent block diagram is displayed in Fig. 11, where $DG = \text{diag}[1, 1]$. Accordingly, f_c is only influenced by Δf_c, while φ_M is only influenced by $\Delta\varphi_M$. K_2^{op} and ω_p^{op} denote base values of K_2 and ω_p, respectively, which are obtained from the analysis in Sect. II-B.

It is worth remarking that the decoupling matrix D is derived from a linearized plant model G evaluated at the nominal operating point and aims at optimizing the dynamics of the auto-tuner. In case of changes in the operating point, it should be adapted to ensure optimal performance; nonetheless, the integrator regulator ensures convergence even in the presence of operating point deviations.

C. Parameters Design

This subsection presents the parameter design of the BPF and the regulator $G_{\tilde{f}}$ of the monitoring block in Fig. 7, as well as the regulators of the auto-tuner in Fig. 11.

The structure of the BPF adopted in Fig. 7 is shown in Fig. 12, and it is implemented using a second-order generalized integrator (SOGI). The bandwidth and dynamics of the BPF depend on k_{sogi}. From the perspective of the magnitude response, the SOGI-based BPF behaves as a first-order system in magnitude for sinusoidal signals with center frequency ω. Hence, its magnitude dynamics can be described by a low-pass filter:

$$G_{Mag\_BPF}(s) = \frac{k_{sogi}\cdot\omega}{2s + k_{sogi}\cdot\omega} \quad (16)$$

Hence, k_{sogi} can be determined by

$$k_{sogi} = \frac{8}{t_s\cdot\omega} \quad (17)$$

where t_s is the settling time of the first-order system. Then $k_{sogi} = 1.4$ is selected in this article [31].

The block AAC includes an LPF for amplitude estimation [29]. Its bandwidth is set to $\omega_{cf} = 2\pi$ rad/s in this article.

For the design of the regulator $G_{\tilde{f}}$, the transfer function between $\tilde{f}$ and $\frac{|x_{out}|}{|x_{in}|}$ is needed, which can be approximated as:

$$T_{monitor}(s) \approx K_{\tilde{f}}\cdot G_{Mag\_BPF}(s)\cdot G_{LPF}(s) \quad (18)$$

where $K_{\tilde{f}}$ is the static gain of the monitor's loop:

$$K_{\tilde{f}} = \left.\frac{\partial\left[\frac{|x_{out}(j2\pi f)|}{|x_{in}(j2\pi f)|} - 1\right]}{\partial f}\right|_{f=\tilde{f}} = \left.\frac{\partial|T(j2\pi f)|}{\partial f}\right|_{f=\tilde{f}} \quad (19)$$

The dynamics of the monitoring loop are mostly determined by G_{Mag_BPF} and G_{LPF}. Then $T_{monitor}$ can be modeled by combining the static gain and the dynamic factors as shown in (18). Hence, the PI regulator $G_{\tilde{f}}$ can be designed based on this uncompensated loop gain $T_{monitor}$.

Based on the analysis in Sect. III-B, the compensated loop gain between f_c and Δf_c, φ_M and $\Delta\varphi_M$ are exactly the regulators $K_{f_c}\frac{1}{s}$, $K_{\varphi_M}\frac{1}{s}$, respectively, because of the adoption of decoupling matrix D which leads to $DG = \text{diag}[1,1]$. The parameters (K_{f_c}, K_{φ_M}) can be directly calculated based on the expected dynamics of the auto-tuner as:

$$K_{f_c} = 2\pi \cdot f_{c\_f}, K_{\varphi_M} = 2\pi \cdot f_{c\_\varphi} \quad (20)$$

where f_{c_f} and f_{c_φ} are the crossover frequency of these two auto-tuning loops, which affect the dynamics of the auto-tuning.

Having cascaded control loops, sufficient bandwidth separation is required to avoid undesired interactions [32]. From the inner to the outer, the nested loops relevant herein are the droop control loop, the monitoring loop, and the auto-tuning loop. The crossover frequency of the droop control loop is initially designed at $4.15\,\text{Hz}$ and it is regulated to the expected value by the auto-tuner when active; then, the performance monitoring loop can be designed with a crossover frequency in the range of $0.5 \sim 1\,\text{Hz}$, and the auto-tuning loop can be designed with a crossover frequency below $0.2\,\text{Hz}$. The inner voltage and current loops of the underlying GFM inverter are extensively discussed in the literature [33] and typically present much faster dynamics than the inner droop loop and do not impact the technique proposed herein.

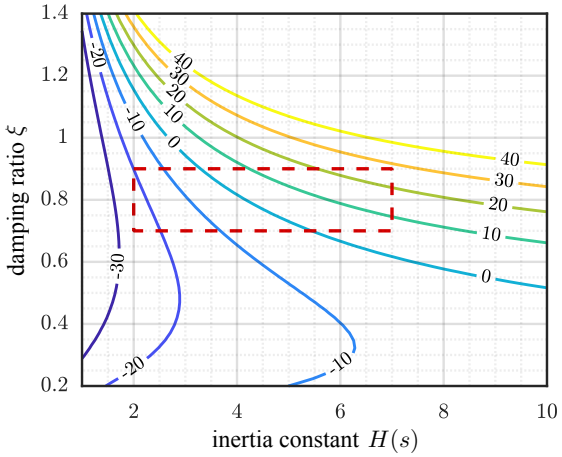

Fig. 13. Error (%) in $\omega_c \approx \omega_n$ approximation in (ξ, H) terms. The red rectangle is the range of interest for the case study.

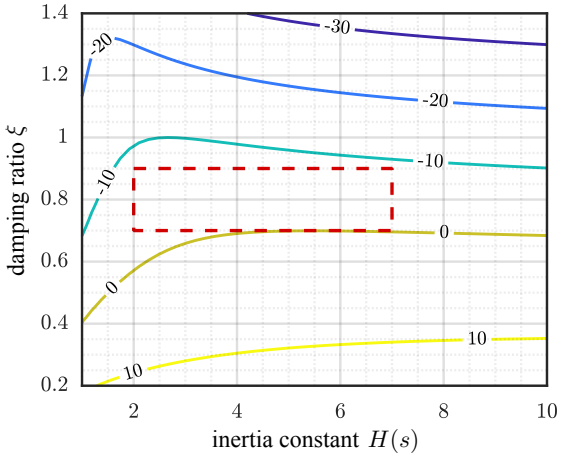

Fig. 14. Error (%) in $\varphi_M(deg) \approx 100 \times \xi$ approximation in (ξ, H) terms. The red rectangle is the range of interest for the case study.

IV. Physical Interpretation of ω_c and φ_M

Grid-forming converter parameters are often described in terms of key physical quantities relevant to traditional synchronous machine dynamics, like the inertia time constant H and the damping ratio ξ. This section establishes an analogy between these quantities and the control parameters considered in this paper.

The system's inertia constant H is defined as the ratio of the kinetic energy stored in the (virtual) rotor to the system's nominal apparent power S_n [34]:

$$H = \frac{J\omega_g^2}{2S_n} \quad (21)$$

where J is the moment of inertia of the virtual rotor and ω_g is the nominal angular frequency. The resulting value of H in seconds is the time the system can sustain its rated power using the stored kinetic energy; it typically ranges from $2\,\text{s}$ to $7\,\text{s}$ [34]. The inertia is implemented based on the swing equation, where the moment of inertia J generating the inertia dynamics can be electrically modeled by a low-pass filter in the droop regulator G_P with a dominant pole at frequency $1/(K_p J \omega_g)$ [35], as adopted in the design choice (11).

Considering the input-output transfer function of the control system in Fig. 3, it yields:

$$\frac{P(s)}{P_{ref}(s)} = \frac{T_{LLF}(s)}{1+T_{LLF}(s)} = \\ = \frac{(K_1+K_2)\omega_p(s/\omega_z+1)\frac{3V_g^2}{X_g}}{s^2 + s(\omega_p + K_2\frac{3V_g^2}{X_g}) + (K_1+K_2)\omega_p\frac{3V_g^2}{X_g}}. \quad (22)$$

The resulting natural frequency ω_n and damping ratio ξ are:

$$\omega_n = \sqrt{(K_1+K_2)\omega_p\frac{3V_g^2}{X_g}} \quad (23)$$

$$\xi = \frac{\omega_p + K_2\frac{3V_g^2}{X_g}}{2\sqrt{(K_1+K_2)\omega_p\frac{3V_g^2}{X_g}}}. \quad (24)$$

The parameters K_1, K_2, and ω_p determine the static droop gain (9), the system damping ratio (24), and can be set to

provide the desired inertia time constant H. It is possible to calculate the crossover frequency ω_c and phase margin φ_M to provide as a reference to the auto-tuner given the desired values of H and ξ. While the relations are generally complex, meaningful relations are obtained considering *i)* typical inertia constants in the literature (e.g., $2\,\mathrm{s} < H < 7\,\mathrm{s}$) [34], *ii)* reasonably underdamped system (e.g., $0.6 < \xi < 0.9$), *iii)* sufficiently separated zero and pole in the used lead-lag filter, and *iv)* sufficiently fast inner voltage and current loops.

Under these assumptions, ω_c and φ_M can be approximated as [36]:

$$\omega_c \approx \omega_n = \sqrt{(K_1 + K_2)\,\omega_p\; 3\,V_g^2/X_g}\,, \tag{25}$$

$$\varphi_M(\mathrm{deg}) \approx 100 \times \xi\,. \tag{26}$$

Accordingly, the crossover frequency depends mainly on the inertia time constant H, and the phase margin mainly on the damping ratio ξ. The approximation errors are evaluated as functions of H and ξ in Fig. 13 and Fig. 14 for the converter used in the case study. The errors in the crossover frequency and phase margin approximations remain below 25% and 10%, respectively, within the range of interest. It is crucial to clarify that these approximations are only used offline by the system designer to translate physical requirements (e.g., desired inertia time constant H and damping ratio ξ) into actionable performance reference values (f_c^{ref} and φ_M^{ref}) for the auto-tuner. Remarkably, neither the effectiveness nor the accuracy of auto-tuning is affected by the approximation errors discussed above.

V. Simulation and Experimental Results

A. Simulation

The effectiveness of the proposed strategy is demonstrated in the following. In particular, a three-phase grid-forming inverter is considered in Matlab/Simulink, equipped with the proposed droop controller with LLF and auto-tuning strategy. The system and controller parameters are listed in Table I, which also applies to the subsequent experimental sections. Based on the analysis in Sect. IV, reference value of control performance indexes are selected as $f_c^{ref} = 5\,\mathrm{Hz}$, $\varphi_M^{ref} = 60°$.

1) Monitoring and auto-tuning processes: Fig. 15 presents the results of the monitoring and auto-tuning processes. During the interval $0\,\mathrm{s}$ to $5\,\mathrm{s}$ the monitoring is deactivated; in such a condition, parameters φ_M and f_c assume initialization values $30°$ and $2\,\mathrm{Hz}$, respectively. From $5\,\mathrm{s}$, the monitor is enabled providing $f_c = 4.15\,\mathrm{Hz}$ and $\varphi_M = 49°$, which match with the results from the analytical relations presented in the previous sections. From $10\,\mathrm{s}$, the auto-tuner is also enabled to adjust the parameters of the droop controller. The desired performance indexes are set to $f_c^{ref} = 5\,\mathrm{Hz}$ and $\varphi_M^{ref} = 60°$. After a transient adjustment lasting about $3\,\mathrm{s}$, the crossover frequency f_c and phase margin φ_M are regulated to the targeted values, which verifies the effectiveness of the proposed auto-tuning strategy.

2) Auto-tuning process under grid-impedance variation: Fig. 16 presents the simulation results of auto-tuning under grid impedance. During the interval $0\,\mathrm{s}$ to $5\,\mathrm{s}$, auto-tuning is already enabled to regulate the crossover frequency and phase margin as reference values: $f_c^{ref} = 5\,\mathrm{Hz}$ and $\varphi_M^{ref} = 60°$. From $10\,\mathrm{s}$, the grid impedance is suddenly changed from $2\,\mathrm{mH}$ to $4.5\,\mathrm{mH}$. After a transient adjustment lasting about $5\,\mathrm{s}$, the auto-tuning restores to the desired values the crossover frequency and phase margin, which verifies the adaptability of the auto-tuning to the variation of grid impedance.

TABLE I
System and Controller Parameters

Parameters	Symbol	Value
Inverter and Grid Parameters		
dc-link voltage	V_{dc}	400 V
dc-link capacitor	C_{dc}	3 mF
Output filter inductor	L_f	950 µH
Output filter capacitor	C_f	12.9 µF
Nominal power rating	S_N	1 kVA
Grid frequency	ω_g	$2\pi \cdot 50$ rad/s
Grid rms voltage	V_g	110 V
Grid impedance	L_g	2 mH
Controller Parameters		
Droop coefficient	K_1	1.301 mrad/(W·s)
Droop coefficient	K_2	0.269 mrad/(W·s)
Pole frequency	ω_p	6.28 rad/s
Zero frequency	ω_z	36.62 rad/s

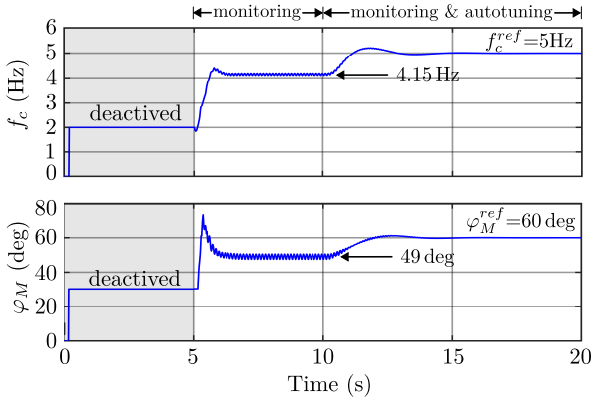

Fig. 15. Simulation results of monitoring and auto-tuning processes.

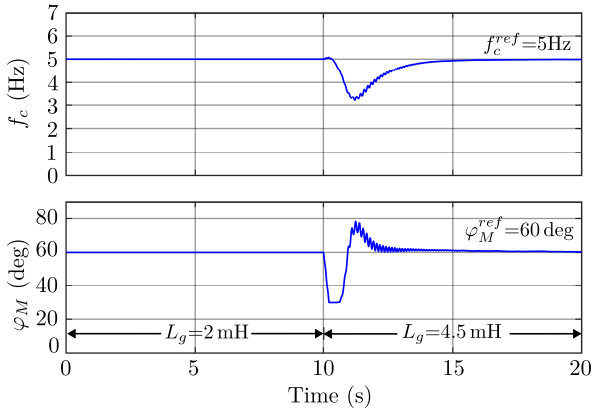

Fig. 16. Simulation results of auto-tuning under grid impedance variation.

B. Experimental Results

To further verify the proposed auto-tuning strategy, experiments are carried out on a three-phase grid-connected inverter

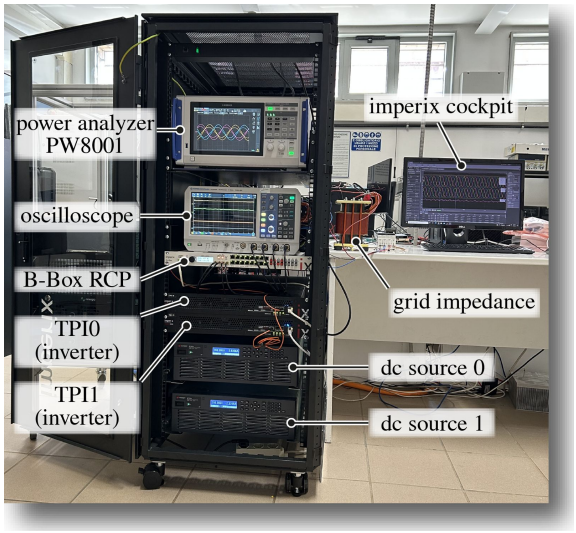

Fig. 17. Experimental setup.

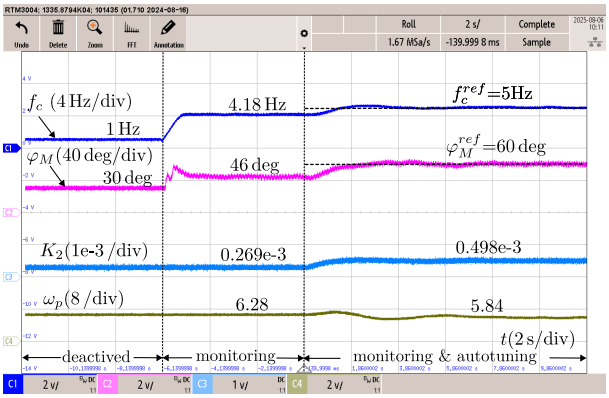

Fig. 18. Experimental results of monitoring and auto-tuning processes.

setup based on Imperix Ltd modules as shown in Fig. 17.

1) Monitoring and auto-tuning processes: Fig. 18 presents the experimental results of monitoring and auto-tuning processes which match well with the simulation results in Fig. 15. After enabling the monitoring and auto-tuning, the crossover frequency f_c and phase margin φ_M are regulated to the expected values, which verifies the effectiveness of the proposed auto-tuning strategy.

2) Auto-tuning process under grid-impedance variation: Fig. 19 presents the experimental results of auto-tuning under grid impedance variation, which present similar waveforms with simulation results in Fig. 16. Even the grid impedance is suddenly changed from $2\ \mathrm{mH}$ to $4.5\ \mathrm{mH}$, the crossover frequency f_c and phase margin φ_M can be maintained at the expected values, which confirms the adaptability of the auto-tuning to the variation of grid impedance.

3) Power step response under different conditions: Fig. 20, Fig. 21, and Fig. 22 present the step responses of the active power loop under three different configurations. Fig. 20 shows the response with $L_g = 2\ \mathrm{mH}$ and enabled auto-tuning. The related performance specifications (i.e., rise time, settling time, and overshoot) are also indicated. Fig. 21 shows the response with $L_g = 4.5\ \mathrm{mH}$ and disabled auto-tuning, with controller

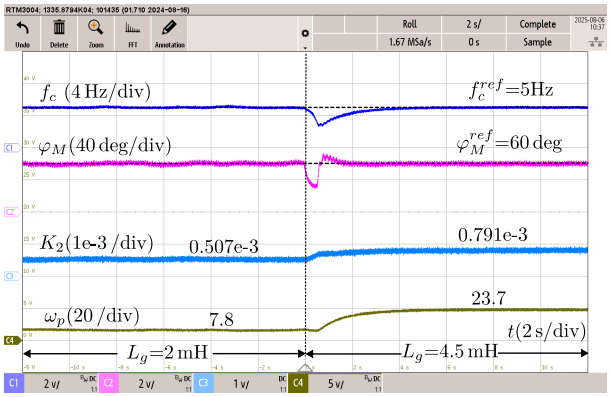

Fig. 19. Experimental results of auto-tuning under grid impedance variation.

parameters tuned for $L_g = 2\ \mathrm{mH}$. Compared with Fig. 20, the increased grid impedance results in longer rise and settling times and a slightly reduced overshoot, indicating degraded dynamics of the active power loop. Fig. 22 shows the response with $L_g = 4.5\ \mathrm{mH}$ and enabled auto-tuning. Compared with Fig. 21, auto-tuning improves the performance specifications: the rise time decreases from $70\ \mathrm{ms}$ to $53\ \mathrm{ms}$, the settling time from $360\ \mathrm{ms}$ to $160\ \mathrm{ms}$, and the overshoot from 18% to 11%. Hence, the dynamics of the active power loop are enhanced by the proposed auto-tuning strategy.

VI. Conclusion

This paper proposes an auto-tuning strategy for droop controllers by adjusting the parameters of an adaptable lead-lag filter. With the proposed control scheme, the crossover frequency and phase margin of the droop control loop can be maintained at desired values by adaptively adjusting the parameters of the lead-lag filter used in the droop control loop. Therefore, the expected control performance of the active power loop can be achieved and maintained, even in the presence of changes or uncertainties in grid impedance. Simulation and experimental results confirm the effectiveness of the proposed strategy.

References

[1] D. Pan, X. Wang, F. Liu, and R. Shi, "Transient Stability of Voltage-Source Converters With Grid-Forming Control: A Design-Oriented Study," *IEEE J. Emerg. Sel. Topics Power Electron.*, vol. 8, no. 2, pp. 1019–1033, 2020.

[2] H. Ruan, Y. Xiao, H. Luo, Y. Yang, M. Molinas, and H. Luo, "Optimized parameter design of grid-following and grid-forming converters for wide operating region," *IEEE Journal of Emerging and Selected Topics in Power Electronics*, vol. 13, no. 4, pp. 5218–5233, 2025.

[3] F. Zhao, T. Zhu, L. Harnefors, B. Fan, H. Wu, Z. Zhou, Y. Sun, and X. Wang, "Closed-Form Solutions for Grid-Forming Converters: A Design-Oriented Study," *IEEE Open Journal of Power Electronics*, vol. 5, pp. 186–200, 2024.

[4] R. Rosso, X. Wang, M. Liserre, X. Lu, and S. Engelken, "Grid-Forming Converters: Control Approaches, Grid-Synchronization, and Future Trends—A Review," *IEEE Open J. Ind. Appl.*, vol. 2, pp. 93–109, 2021.

[5] S. Luo, W. Chen, X. Li, and Z. Hao, "A new virtual inertial strategy for andronov hopf oscillator based grid-forming inverters," *IEEE Journal of Emerging and Selected Topics in Power Electronics*, vol. 12, no. 2, pp. 1995–2005, 2024.

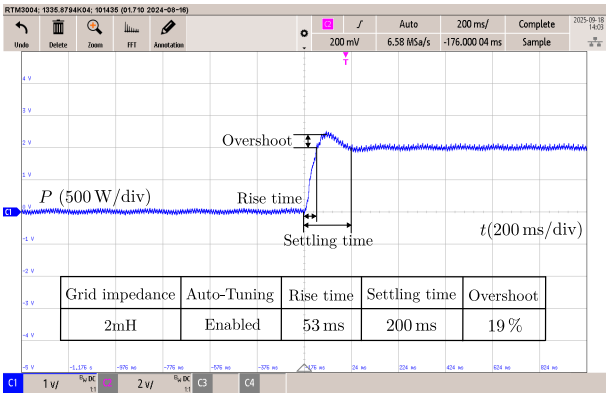

Grid impedance	Auto-Tuning	Rise time	Settling time	Overshoot
2mH	Enabled	53 ms	200 ms	19 %

Fig. 20. Response to $P_{ref} : 0 \rightarrow 1\,\text{kW}$ with $L_g = 2\,\text{mH}$, auto-tuning enabled.

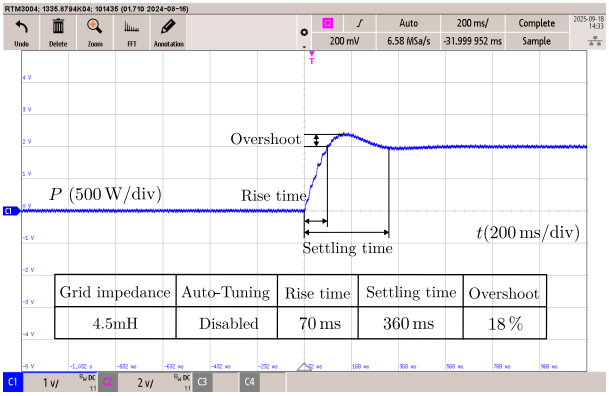

Grid impedance	Auto-Tuning	Rise time	Settling time	Overshoot
4.5mH	Disabled	70 ms	360 ms	18 %

Fig. 21. Response to $P_{ref} : 0 \rightarrow 1\,\text{kW}$ with $L_g = 4.5$ mH, power controller tuned as in Fig. 20 (i.e., parameters tuned for $L_g = 2$ mH). No auto-tuning.

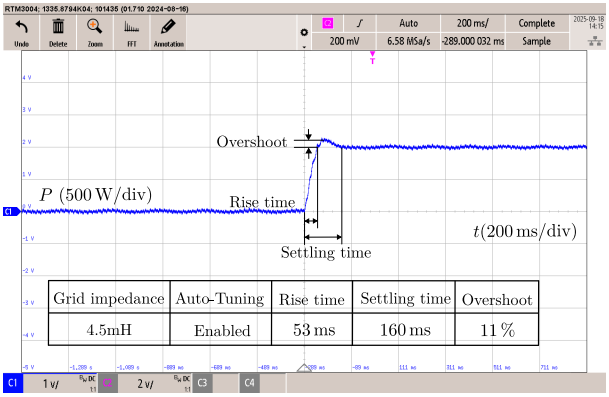

Grid impedance	Auto-Tuning	Rise time	Settling time	Overshoot
4.5mH	Enabled	53 ms	160 ms	11 %

Fig. 22. Response to $P_{ref} : 0 \rightarrow 1\,\text{kW}$ with $L_g = 4.5$ mH and auto-tuning enabled, showing improved performance compared with Fig. 21.

[6] S. Chen, Y. Sun, H. Han, S. Fu, S. Luo, and G. Shi, "A modified vsg control scheme with virtual resistance to enhance both small-signal stability and transient synchronization stability," *IEEE Transactions on Power Electronics*, vol. 38, no. 5, pp. 6005–6014, 2023.

[7] J. Fang, H. Li, Y. Tang, and F. Blaabjerg, "Distributed power system virtual inertia implemented by grid-connected power converters," *IEEE Trans. Power Electron.*, vol. 33, no. 10, pp. 8488–8499, 2018.

[8] N. Pogaku, M. Prodanovic, and T. C. Green, "Modeling, Analysis and Testing of Autonomous Operation of an Inverter-Based Microgrid," *IEEE Trans. Power Electron.*, vol. 22, no. 2, pp. 613–625, 2007.

[9] S. D'Arco and J. A. Suul, "Equivalence of Virtual Synchronous Machines and Frequency-Droops for Converter-Based MicroGrids," *IEEE Trans. Smart Grid.*, vol. 5, no. 1, pp. 394–395, 2014.

[10] W. Zhang, A. M. Cantarellas, J. Rocabert, A. Luna, and P. Rodriguez, "Synchronous power controller with flexible droop characteristics for renewable power generation systems," *IEEE Transactions on Sustainable Energy*, vol. 7, no. 4, pp. 1572–1582, 2016.

[11] W. Zhang, A. Tarraso, J. Rocabert, A. Luna, J. I. Candela, and P. Rodriguez, "Frequency support properties of the synchronous power control for grid-connected converters," *IEEE Transactions on Industry Applications*, vol. 55, no. 5, pp. 5178–5189, 2019.

[12] H. Wu and X. Wang, "Control of grid-forming vscs: A perspective of adaptive fast/slow internal voltage source," *IEEE Transactions on Power Electronics*, vol. 38, no. 8, pp. 10 151–10 169, 2023.

[13] F. Mandrile, V. Mallemaci, E. Carpaneto, and R. Bojoi, "Lead-Lag Filter-Based Damping of Virtual Synchronous Machines," *IEEE Trans. Ind. Appl.*, vol. 59, no. 6, pp. 6900–6913, 2023.

[14] X. Zeng, D. Biadene, Q. Liu, and T. Caldognetto, "Auto-tuning of droop controllers using lead-lag filters for grid-forming inverters," in *2025 IEEE Kiel PowerTech*, 2025, pp. 1–6.

[15] X. Hou, Y. Sun, X. Zhang, J. Lu, P. Wang, and J. M. Guerrero, "Improvement of Frequency Regulation in VSG-Based AC Microgrid Via Adaptive Virtual Inertia," *IEEE Trans. Power Electron.*, vol. 35, no. 2, pp. 1589–1602, 2020.

[16] F. Wang, L. Zhang, X. Feng, and H. Guo, "An Adaptive Control Strategy for Virtual Synchronous Generator," *IEEE Trans. Ind. Appl.*, vol. 54, no. 5, pp. 5124–5133, 2018.

[17] D. Li, Q. Zhu, S. Lin, and X. Y. Bian, "A Self-Adaptive Inertia and Damping Combination Control of VSG to Support Frequency Stability," *IEEE Trans. Energy Convers.*, vol. 32, no. 1, pp. 397–398, 2017.

[18] M. Li, W. Huang, N. Tai, L. Yang, D. Duan, and Z. Ma, "A dual-adaptivity inertia control strategy for virtual synchronous generator," *IEEE Transactions on Power Systems*, vol. 35, no. 1, pp. 594–604, 2020.

[19] F.-J. Lin, K.-H. Tan, X.-Y. Weng, and Y.-R. Li, "An Improved Droop-Controlled Microgrid Using Intelligent Variable Droop Coefficient Estimation," *IEEE Journal of Emerging and Selected Topics in Power Electronics*, vol. 12, no. 4, pp. 4117–4132, 2024.

[20] P. Pant, V. Terzija, T. Hamacher, and V. S. Perić, "Grid agnostic droop control strategy for damping restoration and optimal reactive power sharing," *IEEE Open Journal of Power Electronics*, vol. 6, pp. 613–629, 2025.

[21] J. Guerrero, L. G. de Vicuna, J. Matas, M. Castilla, and J. Miret, "Output impedance design of parallel-connected UPS inverters with wireless load-sharing control," *IEEE Trans. Ind. Electron.*, vol. 52, no. 4, pp. 1126–1135, 2005.

[22] M. Eggers, M. Kaufmann-Bühler, and S. Dieckerhoff, "Accuracy and Stability Assessment of Resistive-Inductive Virtual Impedances for Grid-Forming Converters With LCL Filters," *IEEE Journal of Emerging and Selected Topics in Power Electronics*, vol. 14, no. 2, pp. 2414–2424, 2026.

[23] H. Wu, X. Ruan, D. Yang, X. Chen, W. Zhao, Z. Lv, and Q.-C. Zhong, "Small-signal modeling and parameters design for virtual synchronous generators," *IEEE Transactions on Industrial Electronics*, vol. 63, no. 7, pp. 4292–4303, 2016.

[24] W. Si, J. Fang, X. Chen, T. Xu, and S. M. Goetz, "Transient Angle and Voltage Stability of Grid-Forming Converters With Typical Reactive Power Control Schemes," *IEEE Journal of Emerging and Selected Topics in Power Electronics*, vol. 13, no. 3, pp. 2917–2927, 2025.

[25] J. M. Guerrero, J. C. Vasquez, J. Matas, L. G. de Vicuna, and M. Castilla, "Hierarchical control of droop-controlled ac and dc microgrids—a general approach toward standardization," *IEEE Transactions on Industrial Electronics*, vol. 58, no. 1, pp. 158–172, 2011.

[26] B. Yang, H. Li, S. Xu, H. Liu, and S. Lu, "Systematic Methods to Eliminate the Transient Circulating Powers in the Multi-VSGs System," *IEEE Transactions on Smart Grid*, vol. 15, no. 1, pp. 179–190, 2024.

[27] R. C. Dorf and R. H. Bishop, *Modern Control Systems*, 14th, Ed. USA: Pearson Education, 2022.

[28] R. D. Middlebrook, "Measurement of loop gain in feedback systems," *Int. J. Electron. Theor. Exp.*, vol. 38, no. 4, pp. 485–512, 1975.

[29] A. Khodamoradi, G. Liu, P. Mattavelli, T. Caldognetto, and P. Magnone, "Analysis of an Online Stability Monitoring Approach for DC Microgrid Power Converters," *IEEE Trans. Power Electron.*, vol. 34, no. 5, pp. 4794–4806, 2019.

[30] J. Morroni, R. Zane, and D. Maksimovic, "An Online Stability Margin Monitor for Digitally Controlled Switched-Mode Power Supplies," *IEEE Transactions on Power Electronics*, vol. 24, no. 11, pp. 2639–2648, 2009.

[31] Z. Xin, X. Wang, Z. Qin, M. Lu, P. C. Loh, and F. Blaabjerg, "An improved second-order generalized integrator based quadrature signal generator," *IEEE Transactions on Power Electronics*, vol. 31, no. 12, pp. 8068–8073, 2016.

[32] Q. Liu, T. Caldognetto, and S. Buso, "Review and Comparison of Grid-Tied Inverter Controllers in Microgrids," *IEEE Transactions on Power Electronics*, vol. 35, no. 7, pp. 7624–7639, 2020.
[33] Y. Liao, X. Wang, and F. Blaabjerg, "Passivity-based analysis and design of linear voltage controllers for voltage-source converters," *IEEE Open Journal of the Industrial Electronics Society*, vol. 1, pp. 114–126, 2020.
[34] E. A. S. Ducoin, Y. Gu, B. Chaudhuri, and T. C. Green, "Analytical design of contributions of grid-forming and grid-following inverters to frequency stability," *IEEE Transactions on Power Systems*, vol. 39, no. 5, pp. 6345–6358, 2024.
[35] Z. Yang, S. Lu, and K. Deng, "A novel method to improve the transient performance of virtual synchronous generator by adding a pair of pole-zero in the rotor inertia," in *2020 IEEE 9th International Power Electronics and Motion Control Conference (IPEMC2020-ECCE Asia)*, 2020, pp. 365–371.
[36] G. F. Franklin, J. D. Powell, and A. E. Naeini, *Feedback Control of Dynamic Systems*, 8th ed. Pearson, 2021.

Xiangchen Zeng (Student Member, IEEE) received the B.Sc. and M.S. degrees in electrical engineering from the Qingdao University of Science and Technology, Qingdao, China, in 2021 and Hebei University of Technology, Tianjin, China, in 2024, respectively. He is currently working toward the Ph.D. degree in mechatronics engineering with the University of Padova, Vicenza, Italy. His research interests are in the field of control and stability analysis of grid-connected inverters and the application of artificial intelligence in power electronics.

Tommaso Caldognetto (Senior Member, IEEE) received the M.S. (Hons.) degree in electronic engineering and the Ph.D. degree in information engineering from the University of Padova, Padova, Italy, in 2012 and 2016, respectively. He is currently an Associate Professor with the Department of Management and Engineering, University of Padova, Vicenza, Italy. His research interests include the control of grid-tied converters, microgrid architectures, distributed energy resources, and converters for renewable energy and energy storage integration. He served as an Associate Editor for the IEEE Open Journal of Power Electronics from 2019 to 2026 and has been an Associate Editor for the IEEE Journal of Emerging and Selected Topics in Power Electronics since 2025.

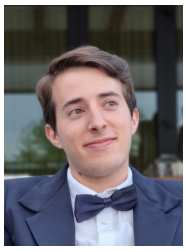

Diego Rigato (Student Member, IEEE) received a bachelor's degree in mechatronic engineering from the University of Padova, Vicenza, Italy, in 2022, and a master's degree in the same field in 2025. His current research focuses on the control of grid-forming converters.

Andrea Lauri (Student Member, IEEE) received the B.Sc. and M.S. degrees in electronics engineering in 2018 and 2022, respectively, from the University of Padova, Padova, Italy, where he is currently working toward the Ph.D. degree in mechatronics engineering.

His current research interests focus on modeling and control of grid-connected inverters in microgrids.

Davide Biadene (Senior Member, IEEE) received the M.S. degree in electronic engineering and the Ph.D. degree in information engineering from the University of Padova, Padova, Italy, in 2014 and 2017, respectively.

He is currently an Assistant Professor at the Department of Management and Engineering, University of Padova, Vicenza, Italy. He was a visiting researcher with the Power Electronic Systems Laboratory, ETH Zurich, Zurich, Switzerland. From 2017 to 2021, he was an Automotive R&D Test Engineer with Infineon Technologies Italia, Padova, Italy. His research interests include power electronics converters, wide-bandgap-based energy conversion systems, and optimization of energy conversion systems for renewable energy, electric mobility, and datacenter applications.

Qing Liu (Member, IEEE) received the B.S. and M.S. degrees in electrical engineering from the School of Automation, Northwestern Polytechnical University, Xi'an, China, in 2012 and 2015, respectively, and the Ph.D. degree from the University of Padova, Padova, Italy, in 2019.

Since 2020, she has been a Researcher with the Department of Electrical Engineering, Hebei University of Technology, Tianjin, China. Her main research interests include low-voltage microgrids and digital control of power electronic converters.